Published in Physical Review Fluids 7, 084602 (2022). © 2022 American Physical Society. https://doi.org/10.1103/PhysRevFluids.7.084602.

# Contributions to pressure drag in rough-wall turbulent flows: insights from force partitioning

Mostafa Aghaei-Jouybari,[1] Jung-Hee Seo,[1] Junlin Yuan,[2] Rajat Mittal,[1,*] and Charles Meneveau[1,†]

[1] *Department of Mechanical Engineering, Johns Hopkins University, Baltimore, MD 21218, USA*

[2] *Department of Mechanical Engineering, Michigan State University, East Lansing, MI 48824, USA*

(Dated: July 14, 2022)

The Force Partitioning Method (Menon and Mittal, JFM 907, A37, 2021) is employed to decompose and analyze the pressure-induced drag for turbulent flow over rough walls. The pressure drag force imposed by the rotation-dominated vortical regions ($Q > 0$, where $Q$ is the second invariant of the velocity gradient tensor) and strain-dominated regions ($Q < 0$) are quantified using a geometry dependent auxiliary potential field (denoted by $\phi$). The analysis is performed on data from direct numerical simulations (DNSs) of turbulent channel flows, at frictional Reynolds number of $\mathrm{Re}_\tau = 500$, with cube and sand-grain roughened bottom walls. Results from both simulations indicate that the Q-induced pressure drag is the largest contributor (more than 50%) to the total drag on the rough walls. Data are further analyzed to quantify the effects of time-mean (coherent) and incoherent turbulent flow on the Q-induced drag force, and to discuss possible effects of roller and U-shaped structures expected to occur at the crest and mid-crest locations of the roughness elements, respectively. Based on the observation that the $\phi$ field encodes information about the surface geometry that directly impacts the drag, we provide initial evidence that it can also be used to parameterize the surface drag. Specifically, we propose and test three norms based on the $\phi$ field (two of them related to the surface-induced potential flow), and explore the characterization of the Nikuradse equivalent sandgrain height $k_s$ based on these parameters for a number of channel flows with different roughness topologies. Data are provided from a suite of DNS cases by Aghaei-Jouybari et al. (JFM, 912, A8, 2021). An empirical correlation depending on these $\phi$-based parameters, with 5 empirically-tuned coefficients, is shown to predict $k_s$ with average and maximum errors of 10.5 and 26 percent, respectively. The results confirm that a purely geometric quantity, the $\phi$-field, provides useful additional information that can be used in drag law formulations.

## I. INTRODUCTION

Turbulence over rough surfaces occurs in many flows, such as atmospheric flows over plant canopies and geomorphology [1, 2], internal flows such as channel and pipe flows [3, 4], external flows past aircraft wings, wind turbine blades [5], ship hulls, and flows in many other applications [6, 7, 8]. The primary effect of a rough wall is its tendency to increase the hydrodynamic drag (except for some particular roughness geometries such as riblets). The drag is mainly caused by viscous effects in low Reynolds number flows and pressure effects at high Reynolds numbers [9, 10]. Readers are referred to Refs. [11, 12, 13] for recent studies quantifying the contribution of each component (viscous and pressure) to the total hydrodynamic drag.

As opposed to the viscous drag, which is generated by regions of high shear rates, the sources of pressure drag are less well understood. In incompressible flows, the pressure field is governed by a Poisson equation ($\nabla^2 P = -2\rho Q$, where $Q$ is the second invariant of the velocity gradient tensor), an elliptic equation, meaning that the pressure at each point inside the domain is influenced by all other points. This fact opens the door for many questions regarding the pressure drag. For example, how is the pressure drag influenced by the vortical structures (where $Q > 0$) and straining motions (where $Q < 0$), happening at different distances from the roughness elements? Or, what are the relative contributions by the mean coherent motions (those persistent in time) and the small scale turbulent motions to the total pressure drag? In the first part of the paper we aim to answer such questions regarding the sources of pressure drag. We use the force partitioning method [FPM, 14, 15, 16, 17], where the main idea is to express the pressure drag, a surface integral ($\int_B P n_1 \mathrm{d}S$), in terms of volume integrals that involve distinct and identifiable effects such as vortex-induction and viscous momentum diffusion. This approach is explained in Sec. II.

Another important aspect of turbulent flow over rough surfaces concerns the quantitative prediction of the drag force using knowledge regarding a characteristic length scale. Already in his seminal work, Nikuradse [18] found that

* Corresponding author; mittal@jhu.edu

† Corresponding author; meneveau@jhu.edu

the logarithmic velocity profile for flow over surfaces under fully rough conditions can be scaled using a characteristic length scale termed the sandgrain roughness height, $k_s$. Moody [19] adopted this idea to connect the hydrodynamic drag coefficient of pipe flows to the characteristic length scale of the wall roughness, resulting in the widely used Moody diagram. Predicting the hydrodynamic drag using a single length scale to characterize the roughness geometry is of great importance in many industrial and engineering applications, and has been the focus of several studies throughout decades [10, 20, 21, 22, 23, 24, 25, 26, 27]. In geophysical and environmental flows [28, 29, 30] the effects of roughness on drag are usually expressed by means of the roughness height $z_0$, also simply related to $k_s$ [see e.g. 10].

There exists, however, a major challenge – that there is no known one-to-one correlation that can accurately and universally predict the length scale ($k_s$ or $z_0$) for a given roughness geometry [31]. Attempts to create physics based correlations include [25, 26, 27, 32, 33, 34], among others. Data driven approaches have also been explored, such as a recent study by Aghaei-Jouybari *et al.* [35] that used machine learning to predict $k_s$. They trained a neural network which used 9 geometric and statistical parameters (such as height skewness, slope, etc.) as inputs. For network training, they employed a database of diverse roughness geometries, including 30 DNSs and 15 experimental flows, all identified to be in the fully rough regime. The trained network (including 3 layers with 18, 7 and 7 nodes in each layer) was able to predict $k_s$ with average and maximum errors of less than 10 and 30 percent, respectively.

Further improvements in predictive capabilities should be possible if one could better connect surface geometric features to flow structures and then relate those to the drag force acting on the rough surface. A number of studies have identified particular flow structures that occur near roughness elements in rough wall boundary layers. For narrow-bandwidth rough walls (where one scale of the roughness is dominant), Talapatra and Katz [36] identified U-shape structures that wrap around roughness elements (pyramids in their case) and are lifted from the surface due to upward velocity induced by the legs of the adjacent structures. In the case of cube roughness, Aghaei-Jouybari *et al.* [37] noticed that the heads of these structures are separated from the legs at the crest location, due to high effective shearing, so that the structures roll over the roughness elements. This behavior causes a shortened streamwise length scale of the coherent motions, reinforcing the dissipative scales and possibly affecting drag. Away from the wall in the outer flow, one expects to see whole or partial hairpins structures [38], similar to those in smooth-wall flows due to the outer layer similarity [39]. Quantitatively relating surface geometric properties and flow structures to hydrodynamic drag forces can be accomplished using the FPM, which as explained in more detail in Sec. II, involves a potential scalar field $\phi(\mathbf{x})$ that connects the surface geometry to flow structures in the bulk of the flow. Since $\phi(\mathbf{x})$ depends only upon the surface geometry it may provide additional information about the surface, useful in predicting roughness length scales.

There are two main objectives in this study. First, to decompose the hydrodynamic drag down to its fundamental components and to relate it to flow structures occurring in the bulk of the flow. As shown later, the properties of the scalar potential field $\phi$ will be crucial to understand the effects of flow structures on the hydrodynamic drag. The second objective is to illustrate that the newly introduced potential field $\phi$, that depends on roughness geometry only, may also be used to define additional parameters in models to predict the equivalent sandgrain roughness height.

As will be fully explained in Sec. II, the FPM is derived from the Navier-Stokes (NS) equations, and can, in-principle, exactly quantify the contribution of each vortex or strain-dominated regions to the pressure drag. Analysis of DNS data of fully developed channel flows over a regular array of aligned wall-mounted cubes and randomly oriented sand-grain elements are presented in Secs. III A and III B, respectively, and a number of generic trends associated with the effects of $Q$-induced motions on the pressure drag are identified. Having shown that the FPM provides interesting insights into the correlations among flow structures and hydrodynamic drag via the potential function $\phi$, the latter is employed to examine several statistical geometric parameters based on $\phi$ and its spatial gradients across the domain. These parameters are then used to propose a correlation for the sandgrain roughness height $k_s$ involving several adjustable parameters that are fitted based on data. Results are presented in Sec. IV, while conclusions for this study are summarized in Sec. V.

## II. FORCE PARTITIONING METHOD

Following Menon & Mittal [17] we use FPM to partition and quantify the contribution of rotation and strain-dominated regions to the total hydrodynamic drag (see the schematic of Fig. 1). A vortex-dominated region (Fig. 1a) is identified as a region where $Q > 0$, and similarly a strain-dominated region occurs where $Q < 0$ (Fig. 1b). If a vortex filament emerges upstream and sufficiently close to a roughness element (location A) it opposes the hydrodynamic drag, and if it happens downstream of a roughness element (location B) it increases the drag. Vice-versa, if a strain-dominated region emerges at location A, it contributes to the hydrodynamic drag, while if it occurs at location B, it reduces the net drag. The physical reason behind these is rather straightforward [17]– regions with $Q > 0$ correspond to the cores of vortical structures where the local pressure is lower than values at surrounding points. Therefore, a vortex would decrease(increase) the drag if it happens in the upstream(downstream) of a roughness element. Regions

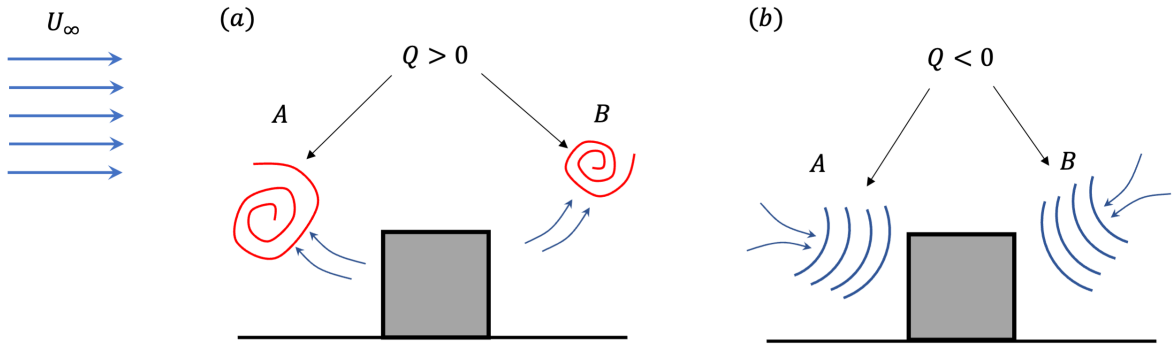


FIG. 1. Schematics of drag generation and annihilation by vortex-dominated ($Q > 0$, a) and strain-dominated ($Q < 0$, b) regions in the bulk of the flow.

with $Q < 0$ correspond to strain-dominated regions where streamlines have tendency to block each other and form pseudo-stagnation regions, causing the pressure to be locally higher than the surrounding points. These regions of the flow would increase(decrease) drag if they occur upstream(downstream) of a roughness element.

The starting point of FPM [14] is the calculation of an auxiliary potential field $\phi$, which obeys the Laplace equation ($\nabla^2\phi = 0$) with a Neumann boundary condition solely dependent on the solid body geometry and the direction of the force one wishes to partition. Thus for the $i^{th}$ direction, the auxiliary potential $\phi_i$ satisfies the following equation:

$$\boldsymbol{\nabla}\phi_i \cdot \boldsymbol{n} = \begin{cases} n_i & \text{on } B, \\ 0 & \text{on } \Sigma. \end{cases} \tag{1}$$

Here $B$ represents the flow exposed boundary of the solid body (in our case roughness) that FPM is applied to and $\Sigma$ expresses all other boundaries. Also, $\boldsymbol{n}$ is the unit normal vector (positive into the solid) and $i = 1, 2, 3$ is the direction of the decomposed force. Note that with these specified properties, $\phi_i$ is a surface dependent field that does not depend on the flow field and that can be obtained using standard numerical techniques for any given surface. For examining the force in an arbitrary direction characterized by a unit vector $\boldsymbol{e}$, $n_i$ in Eq. 1 can be simply replaced by $\boldsymbol{n} \cdot \boldsymbol{e}$. This study focuses on drag, i.e, the $i = 1$ direction, and we will dispense with the subscript $i$ in the remaining discussion while indicating the $i = 1$ direction of the surface normal as $n_1$.

By performing an inner product between the NS equations and $\boldsymbol{\nabla}\phi$, and integrating in the entire fluid volume $V$, one obtains:

$$\int_V \boldsymbol{\nabla}P \cdot \boldsymbol{\nabla}\phi \, \mathrm{d}^3\boldsymbol{x} = -\int_V \rho\left(\frac{\partial \boldsymbol{u}}{\partial t} + \boldsymbol{u}\cdot\boldsymbol{\nabla}\boldsymbol{u} - \nu\nabla^2\boldsymbol{u}\right)\cdot\boldsymbol{\nabla}\phi \, \mathrm{d}^3\boldsymbol{x}, \tag{2}$$

where $\boldsymbol{u}$, $P$, $\rho$ and $\nu$ are, respectively, the velocity vector, pressure, fluid density and fluid kinematic viscosity. The left hand side of Eq. (2) is converted to a surface integral using ($\boldsymbol{\nabla}P\cdot\boldsymbol{\nabla}\phi = \boldsymbol{\nabla}\cdot(P\boldsymbol{\nabla}\phi) - P\nabla^2\phi$). Further rearranging the right hand side of Eq. (2) using properties of $\phi$ and the incompressibility constraint, and noting the connection between the divergence of the non-linear term and the quantity $Q$ [17] one obtains the following for a flow with stationary boundaries:

$$\underbrace{\int_B Pn_1 \mathrm{d}S}_{F_1^p} = \underbrace{-2\rho\int_V \phi\, Q \, \mathrm{d}^3\boldsymbol{x}}_{F_Q} + \underbrace{\mu\int_V \nabla^2\boldsymbol{u}\cdot\boldsymbol{\nabla}\phi \, \mathrm{d}^3\boldsymbol{x}}_{F_\nu}, \tag{3}$$

where $F_1^p$ is the total pressure force exerted on the surface $B$ in the streamwise direction, $F_Q$ is the so-called $Q$-induced force ($Q$ is defined as usual as $Q = -0.5u_{i,j}u_{j,i}$, where $u_{i,j} = \partial u_i/\partial x_j$), and $F_\nu$ is the viscous momentum diffusion induced pressure force. We have also assumed stationary total momentum in the volume so that the volume integral of $\partial\boldsymbol{u}/\partial t$ has been neglected.

The volume integrals in Eq. (3) enable us to calculate the contributions to pressure drag arising from any arbitrary region in the bulk of the flow. The force densities $f_Q \equiv -2\rho\,\phi Q$ and $f_\nu \equiv \mu\nabla^2\boldsymbol{u}\cdot\boldsymbol{\nabla}\phi$ are central to the FPM decomposition and will be analyzed alongside the integrals over the entire flow volume in the following sections.

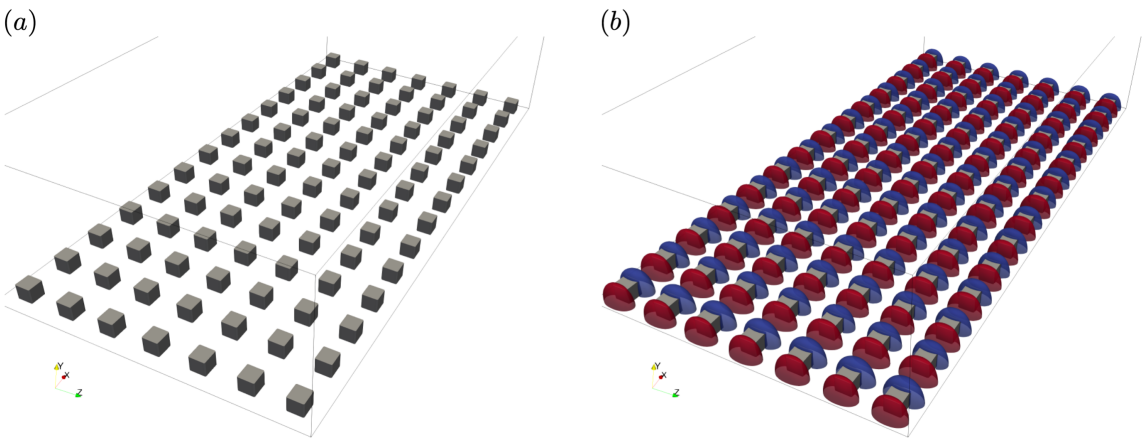


FIG. 2. Cubical roughness elements (a), and iso-surfaces of $\phi$ (b), $\phi = +0.01$ (red bulb-like surface) and $\phi = -0.01$ (blue bulb-like surface).

Considering that the $Q$-criterion is a well-known vortex identification method, the integrand $f_Q$ shows direct effects of the vortex dominated regions ($Q > 0$) and strain dominated regions ($Q < 0$) on the pressure drag. While we follow the approach of [17] most closely, additional details and earlier applications of FPM-like analyses can be found in Refs. [14, 15, 16].

## III. RESULTS

The FPM analysis is performed for two roughness topographies, a cubical roughness in Sec. III A and a sand-grain roughness in Sec. III B. For both cases a DNS is performed for a fully-developed periodic channel flow at frictional Reynolds number of $\mathrm{Re}_\tau = 500$ with roughened bottom wall and smooth top wall. The DNSs are performed using the in-house ViCar3D code [40, 41] that is based on a fractional step method. The solver employs a second-order spatial central-difference discretization as well as a second order Adams-Bashforth time advancement scheme to solve the NS equations. The pressure Poisson equation is solved using scheduled relaxation Jacobi (SRJ) method [42]. Both the solver and the immersed boundary method have been extensively validated and employed in several applications previously [40, 41]. The length, height and width of the channel are $8\delta$, $2\delta$ and $4\delta$, respectively ($\delta$ being the channel half-height) for both cases. The respective grid resolutions in viscous units are $\Delta x^+ = 8$, $\Delta y^+_{max} = 4.5$ (with the first 3 grid points below $y^+ = 1$ and $\Delta y^+ = 0.44$ at the crest location $y = k_c$) and $\Delta z^+ = 10$. Both simulations ran for $28T$ (where $T = \delta/u_\tau$ is a large eddy turn over time) to reach the stationary turbulence and then flow statistics were gathered for at least $10T$.

Here, we first examine FPM results for cube case in Sec. III A and then the results will be compared with those of sand-grain in Sec. III B, focusing on the main similarities and differences between these two widely-different roughness topographies.

### A. Cube

Figure 2 shows the cubical roughness geometry and isosurfaces of the associated $\phi$ field. In total 98 cube elements of height $k_c = 0.2\delta$ were mounted on the bottom wall, 14 rows in $x$ and 7 rows in $z$ directions. The height of the cubes in viscous units is $k_c^+ = 100$ and the flow can therefore be considered to be in the fully rough regime [10, 43].

Figure 3 shows contours of $u$, $Q$, $\phi$, $f_Q$ and $f_\nu$ at an instantaneous time snapshot. As the figure shows, $\phi$ is positive in front of each roughness element and negative at the back of the elements. Therefore, one infers that vortex dominated regions ($Q > 0$) contribute to drag when they occur at the back of a roughness element (in significant negative $\phi$ regions), but they decrease the drag if they occur in front of an element (in significant positive $\phi$ regions). The trend for strain dominated regions ($Q < 0$) is the opposite, namely they contribute to drag if they occur in front of an element and they decrease the drag if they occur at the back of an element. Furthermore, if we zoom in on the roughness sublayer (displayed on the left column of the figure) and extract one vortex filament (encircled in $Q$ contour), we notice that the left portion of this vortex produces a drag force since it is closer to the upstream

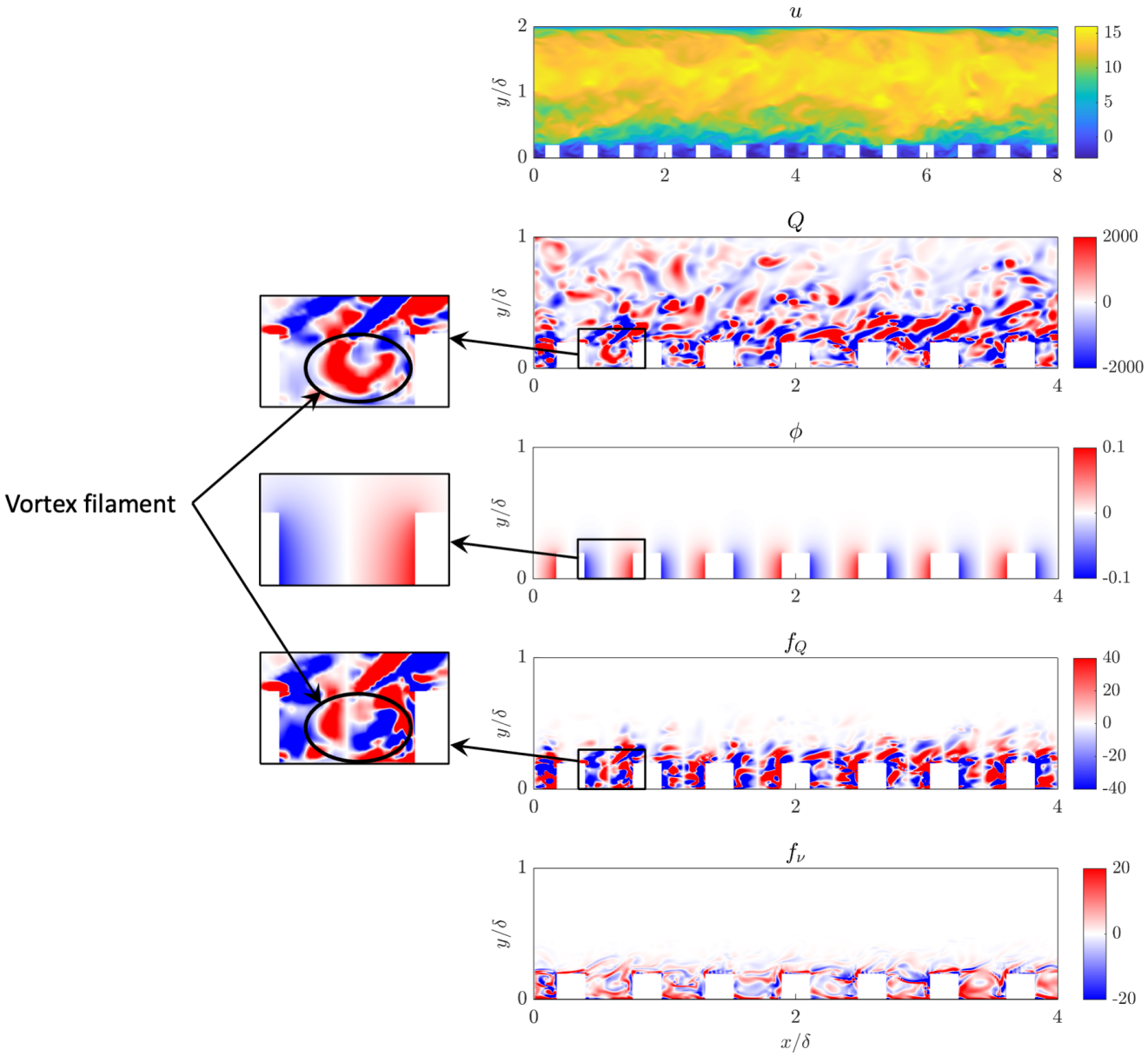


FIG. 3. Contours of instantaneous $u$, $Q$, $\phi$ (constant in time), $f_Q$ and $f_\nu$. A vortex structure cross-section is encircled in the zoomed in figures of $Q$ and $f_Q$.

roughness element and the right portion opposes the drag since it is closer to the downstream element. These are evident from the respective $f_Q$ contour. The FPM therefore allows us to identify the drag generating and annihilating portions from even a single vortex filament.

Next, we can compute the volume integrals of the pressure force components $F_Q$ and $F_\nu$ over the entire flow volume along with the surface integrals of the shear forces. The results are shown in Fig. 4, where five sources for the total drag can be identified. Their respective contributions for this particular kind of roughness at the Reynolds number

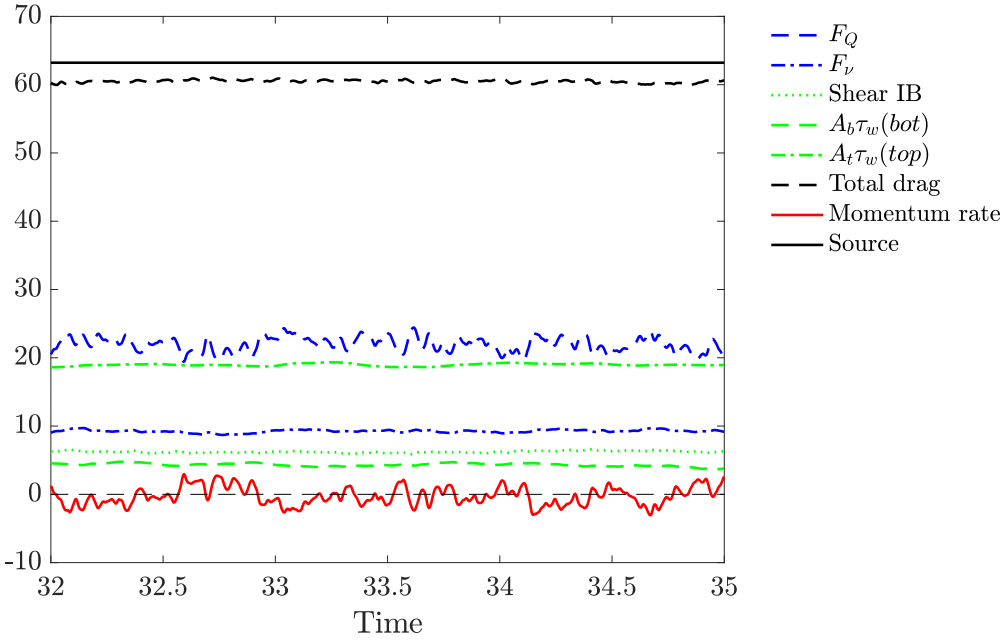


FIG. 4. Decomposition of the total hydrodynamic drag as function of time. $A_b$ and $A_t$ are, respectively, the area of the regions not covered by cubes in the bottom wall and the area of top wall. "Momentum rate" refers to the volume integral of the unsteady term in NS equations. Considering the simulation is done in a constant pressure gradient mode, the mass flux inside the channel is not exactly constant (although being statistically stationary) and its time derivative fluctuates around zero. The average contribution by this term is small (less than 1%), as expected.

of the simulation are:

Total drag =

Q-induced pressure drag on roughness elements ($F_Q$) (= 21.99; 52.6% of total drag on bottom wall)
+ Viscous diffusion induced pressure drag on roughness elements ($F_\nu$) (= 9.25; 22.1% of total drag on bottom wall)
+ Shear drag on surfaces of roughness elements (= 6.23; 14.9% of total drag on bottom wall)
+ Shear drag on bottom wall, non-roughened parts (= 4.31; 10.4% of total drag on bottom wall)
+ Shear drag on top wall (= 18.97)
= 60.75 (on average)

The total drag force should balance the total momentum source in an equilibrium channel flow with stationary turbulence. The total source term is $-\frac{\partial \overline{P}}{\partial x}V = 63.2$ (normalized by $\delta$ and the friction velocity), where $-\frac{\partial \overline{P}}{\partial x} = 1$ was imposed on the right hand side of the streamwise component of NS equations to drive the flow in this direction. The associated difference between the total momentum source and the total drag force is less than 5%. The sources of the momentum budget discrepancy can be traced mostly to discretization errors in evaluating $Q$ from velocity gradients, and from numerical integration. We consider this level of discrepancy to be sufficiently small for the purposes of the present study.

Note that the total drag force on the roughness side of the channel—sum of $F_Q$, $F_\nu$, the shear force on the roughness surface and the bottom wall shear—contributes to 68.8% of the total drag, in which the $Q$-induced force $F_Q$ is the largest contributing factor to both the rough wall drag (52.6%) and the total drag. Also the contribution from $F_\nu$ is almost equal to the total shear drag exerted on the bottom wall (on both roughened and non-roughened parts).

To examine these forces in more detail, we can make use of their volume-integral nature and perform a conditional averaging analysis based on different spatial events. Each force is first conditionally averaged based on four conditions: $Q > 0$ and $\phi > 0$ (contribution of vortex-dominated regions upstream of the roughness elements), $Q < 0$ and $\phi > 0$ (strain-dominated, upstream), $Q > 0$ and $\phi < 0$ (vortex-dominated, downstream), and $Q < 0$ and $\phi < 0$ (strain-dominated, downstream), then multiplied by the condition probability. The latter is necessary to quantify the actual contribution of each event to the total drag. The results are shown in Fig. 5 for both $F_Q$ and $F_\nu$. Upstream of a roughness element (where $\phi > 0$) strong generation and annihilation of $F_Q$ occurs, respectively, by strain-dominated

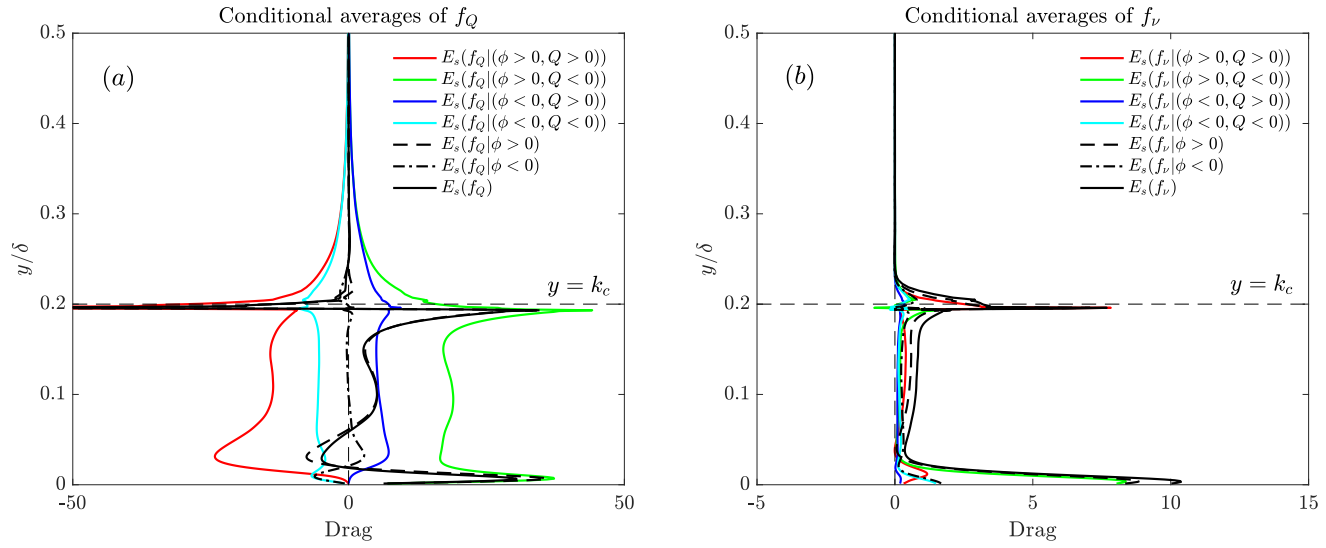


FIG. 5. Weighted conditional averages of $F_Q$ (a) and $F_\nu$ (b) based on four events: i) $\phi > 0$ and $Q > 0$ (vortex-dominated region, upstream of the cube elements) ii) $\phi > 0$ and $Q < 0$ (strain-dominated, upstream) iii) $\phi < 0$ and $Q > 0$ (vortex-dominated, downstream) and iv) $\phi < 0$ and $Q < 0$ (strain-dominated, downstream). Please note we plot the weighted conditional averages $E_s$ to accurately quantify the contribution of each event to the total drag. Here $E_s(\text{event}) = E(\text{event}) \times P(\text{event})$, where $E$ and $P$ are the true (intrinsic) conditional averages and probability of an event. Also note $E_s(f|\phi > 0) = E_s(f|(\phi > 0, Q > 0)) + E_s(f|(\phi > 0, Q < 0))$, shows contribution of the upstream events to the respective force, and $E_s(f|\phi < 0) = E_s(f|(\phi < 0, Q > 0)) + E_s(f|(\phi < 0, Q < 0))$ shows contribution of the downstream events. The total drag per volume is shown by the solid black lines $E_s(f)$.

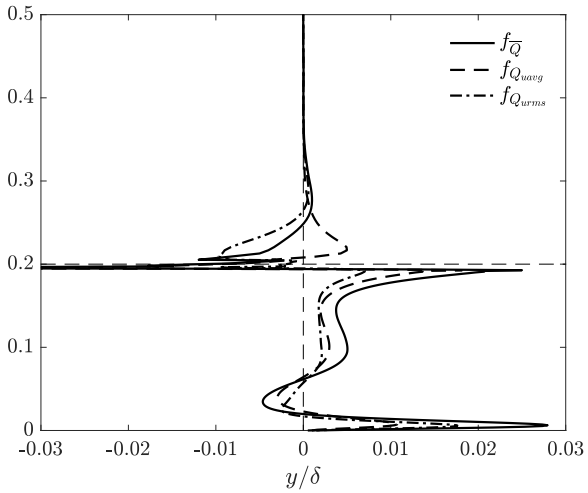


FIG. 6. Contribution to drag by $\overline{Q} = -0.5\overline{u_{i,j}u_{j,i}}$ (note $u_{i,j} = \frac{\partial u_i}{\partial x_j}$), $\overline{Q}_{uavg} = -0.5\overline{u}_{i,j}\overline{u}_{j,i}$ and $\overline{Q}_{urms} = -0.5\overline{u'_{i,j}u'_{j,i}}$. Their respective forces are $f_{\overline{Q}}$, $f_{Q_{uavg}}$, and $f_{Q_{urms}}$, intrinsically averaged in both time and $x$-$z$ plane. Note $F_Q = \int A_f f_{\overline{Q}} dy = 22.0$, $F_{Q_{uavg}} = \int A_f f_{Q_{uavg}} dy = 12.3$ $(= 0.56F_Q)$ and $F_{Q_{urms}} = \int A_f f_{Q_{urms}} dy = 9.7$ $(= 0.44F_Q)$, all normalized by $\delta$ and $u_\tau$. Also $A_f$ is the planar fluid occupied area.

and vortex-dominated regions (Fig. 5a), and the net effect (sum of the red and green curves, black dash line) is the balance between these two strong opposing forces. The roles of vortex-dominated and strain-dominated regions switch downstream of the roughness elements (where $\phi < 0$), but their net effect is almost zero. One, therefore, concludes that the net $F_Q$ is predominantly determined by the events upstream of the roughness elements, where $\phi > 0$. Figure 5(b) shows the conditional averaging for $F_\nu$ based on the same events. Here, although the contribution from each event is small in magnitude (compared to their respective values in $F_Q$ plot), all of them are positive, irrespective of

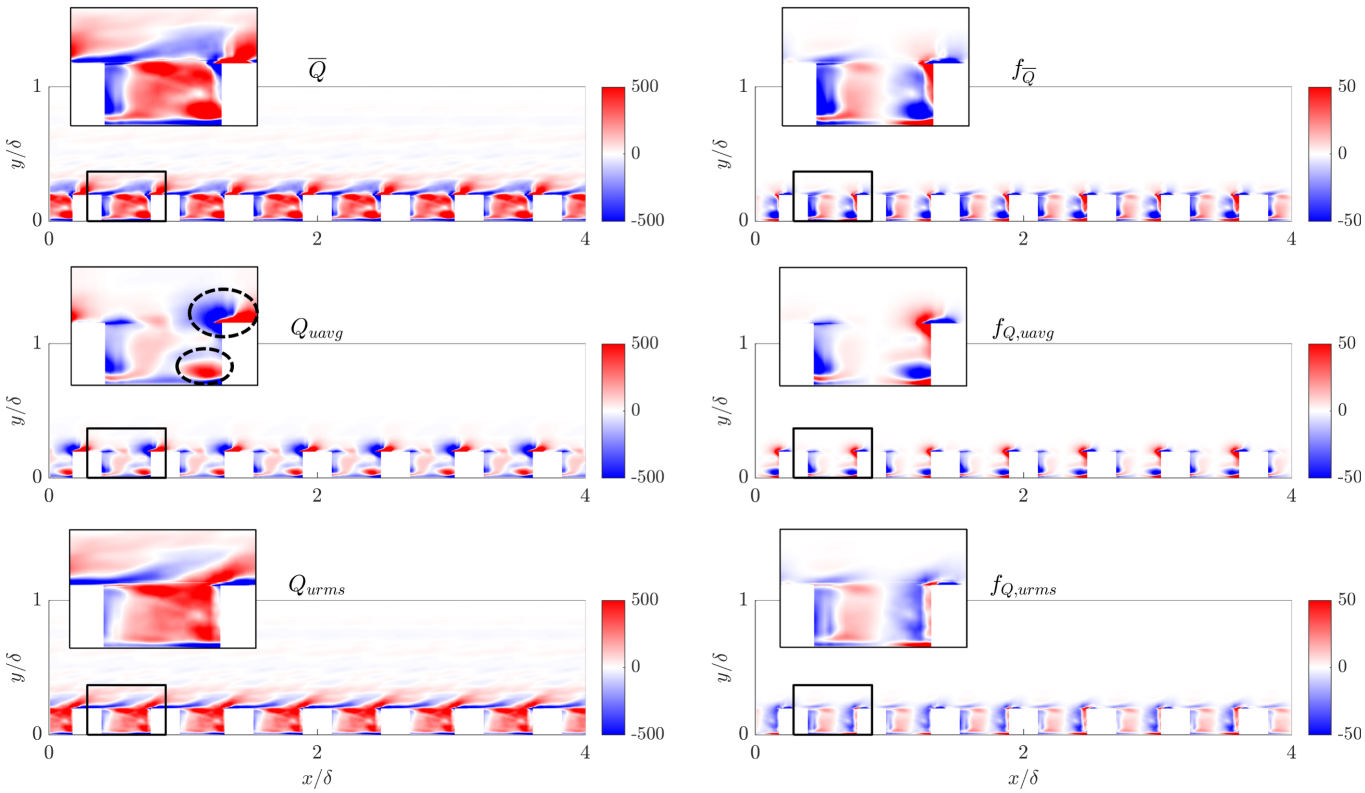


FIG. 7. Contours of $\overline{Q} = -0.5\overline{u_{i,j}u_{j,i}}$, $\overline{Q}_{uavg} = -0.5\overline{u}_{i,j}\overline{u}_{j,i}$ and $\overline{Q}_{urms} = -0.5\overline{u'_{i,j}u'_{j,i}}$ with their respective forces $f_{\overline{Q}}$, $f_{Q_{uavg}}$, and $f_{Q_{urms}}$. All quantities are time averaged and phase averaged over each cube element. Possible signatures of U-shape structures (occurring around $y = 0.5k_c$) and roller structures or turbulent motions generated in the thin shear layer above the cubes (occurring at $y = k_c$) are encircled in the contour of $Q_{uavg}$.

the event type (vortex or strain-dominated) or location (upstream or downstream of the elements). That is why the net $F_\nu$ contributes a non-negligible 22.1% to the rough wall drag.

We next address the question whether the drag is dominated by the $Q$ parameter associated with the mean flow or by the turbulence. In Fig. 6 we show time-averaged contribution to drag by $\overline{Q} = -0.5\overline{u_{i,j}u_{j,i}}$, $\overline{Q}_{uavg} = -0.5\overline{u}_{i,j}\overline{u}_{j,i}$ and $\overline{Q}_{urms} = -0.5\overline{u'_{i,j}u'_{j,i}}$, with their respective $Q$-induced forces $\overline{f}_Q$, $f_{Q,uavg}$ and $f_{Q,urms}$. There are three peaks (two positives and one negative) in the figure, the negative one happening around $y \approx 0.5k_c$ while the others are near the crest $y \approx k_c$ and very near the bottom surface. The negative peak is possibly attributed to the head-down U-shape structures described by Talapatra and Katz [36] that wrap around roughness elements, while the peak near the top may be attributed to roller mechanism [37] that happens right on the crest before the flow is detached from the surface or due to turbulence generated in this region of strong shear. The one near the bottom surface is likely due to the strong shear existing there as well. These flow patterns are persistent in time and thus contribute to the time-averaged velocity field, leading to about 56% of $F_Q$ attributed to $\overline{Q}_{uavg}$. Signatures of these patterns may be found in the time-averaged contour plots of $Q_{uavg}$ and $f_{Q_{uavg}}$ in Fig. 7. Also, from contours of $Q_{urms}$ and $f_{Q_{urms}}$ in Fig. 7 one notices generation of turbulent motions in the wake of roughness elements and their contribution to the total drag, which has been quantified to be 46% of the total $F_Q$.

### B. Sandgrain

The sand-grain roughness topography and the associated $\phi$-field are shown in Fig. 8 (a) and (b), respectively. In total 117 sandgrain elements, 13 rows in $x$ and 9 rows in $z$ directions, are mounted on the bottom wall. Each element is a randomly oriented semi-ellipsoid with semi axes of $0.7k_c$, $k_c$ and $0.5k_c$ in streamwise, wall-normal and spanwise directions, respectively. Similar to the cube case, for the sandgrain roughness elements $k_c = 0.2\delta$ is chosen. As expected, the $\phi$ iso-surfaces in Fig. 8(b) are more distorted than their cube counterparts, due to inherent randomness in the sand-grain roughness geometry. Note that the iso-surfaces shown are less concentrated for elements near the

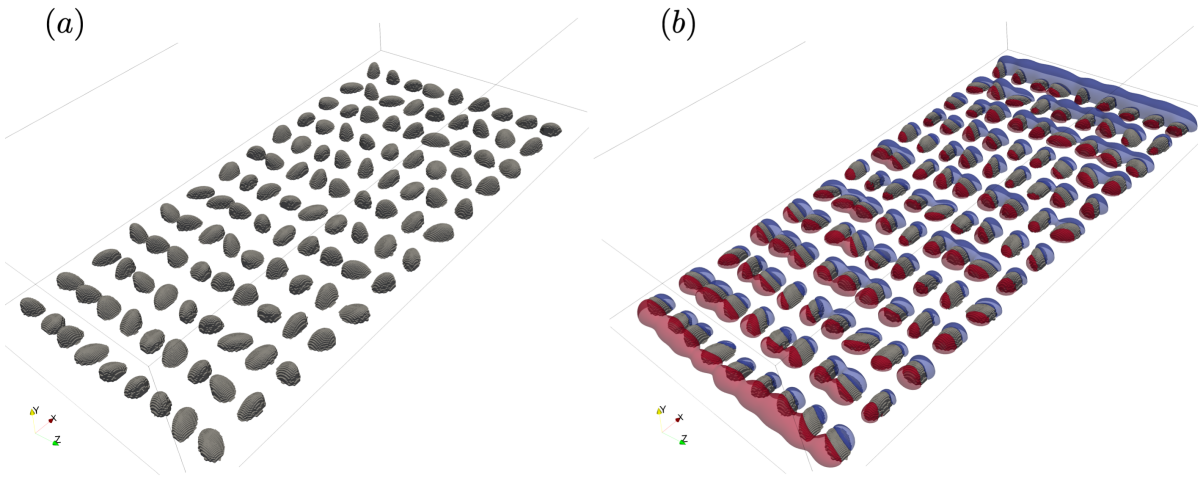


FIG. 8. Sand-grain roughness elements (a), and iso-surfaces of $\phi$ (b), $\phi = +0.02$ (red surfaces) and $\phi = -0.02$ (blue surfaces).

inlet and outlet due to the fact that the distance between elements along the streamwise direction implied by the periodic boundary condition is slightly larger. This issue does not affect any of the analysis and results presented.

Most of the conclusions made for the cube roughness are also true for the sand-grain one, with subtle differences due to different topographies. Fig. 9 shows the instantaneous contours of $u$, $Q$, $\phi$ (constant in time), $f_Q$ and $f_\nu$ for the sand-grain roughness. Similar to the cube case in Fig. 3 a vortex filament ($Q > 0$) upstream of and close enough to the roughness elements ($\phi > 0$) annihilates drag while a strain-dominated region ($Q < 0$) increases drag in the same location. Their roles are reversed downstream of the roughness elements where $\phi < 0$. The contribution of each component to the total drag is listed below

Total drag =
Q-induced pressure drag on roughness elements ($F_Q$)(=25.51, 52.7% of total drag on bottom wall)
+ Viscous diffusion induced pressure drag on roughness elements ($F_\nu$) (=11.16, 23.1% of total drag on bottom wall)
+ Shear drag on surfaces of roughness elements (=8.50, 17.5% of total bottom drag)
+ Shear drag on bottom wall, non-roughened parts (=3.24, 6.7% of total bottom drag)
+ Shear drag on top wall (=18.45)
= 66.86 (on average)

The average source driving the flow in the streamwise direction is $-\frac{\partial \overline{P}}{\partial x}V = 63.31$, thus the FPM error for the force budget for the sand-grain surface is 5.6%. The relative significance of the $Q$-induced force $F_Q$ is quite similar to its cube counterpart, contributing more than 50% of the total rough-wall drag also for the sand-grain case.

Fig. 10 shows the conditional averages of $F_Q$ and $F_\nu$ based on the same four events as used in the decomposition shown in Fig. 5. The same conclusions as those in Fig. 5 are applicable here too, with one major difference in qualitative trends: there is no sharp peak in the conditional profiles of $F_Q$ at the roughness crest location $y = k_c$. The more smoothed behavior of the conditional averages is due to the fact that the roughness element top surface is not at a single height but is distributed. Also, the fact that the profile peaks happen at $y = 0.5k_c$ suggest that there are less incidences of roll-over turbulent structures for the sandgrain case as opposed to the cube case, leaving U-shaped structures to dominate drag generation for the sand-grain roughness.

The foregoing analysis shows that the major contributions to pressure drag arise from regions with $\phi > 0$ and that significant cancellations occur within those regions. The total pressure drag depends on the preponderance of positive or negative values of $Q$ within those regions. Since the values of $Q$ there depend on the flow and cannot be deduced or assumed without detailed solutions and simulations of the entire flow field, prediction of total drag based only on the distribution of $\phi$ would appear to be quite challenging. However, some important trends can be expected: The larger the values of $\phi$ in certain regions near the surface the larger the drag force. Also, the larger spatial variability of $\phi$ across the domain, the more likely large drag forces can be obtained. In Sec. IV we explore various statistical features of the spatial distribution of $\phi$ and aim to correlate these to roughness length characterizing the drag force.

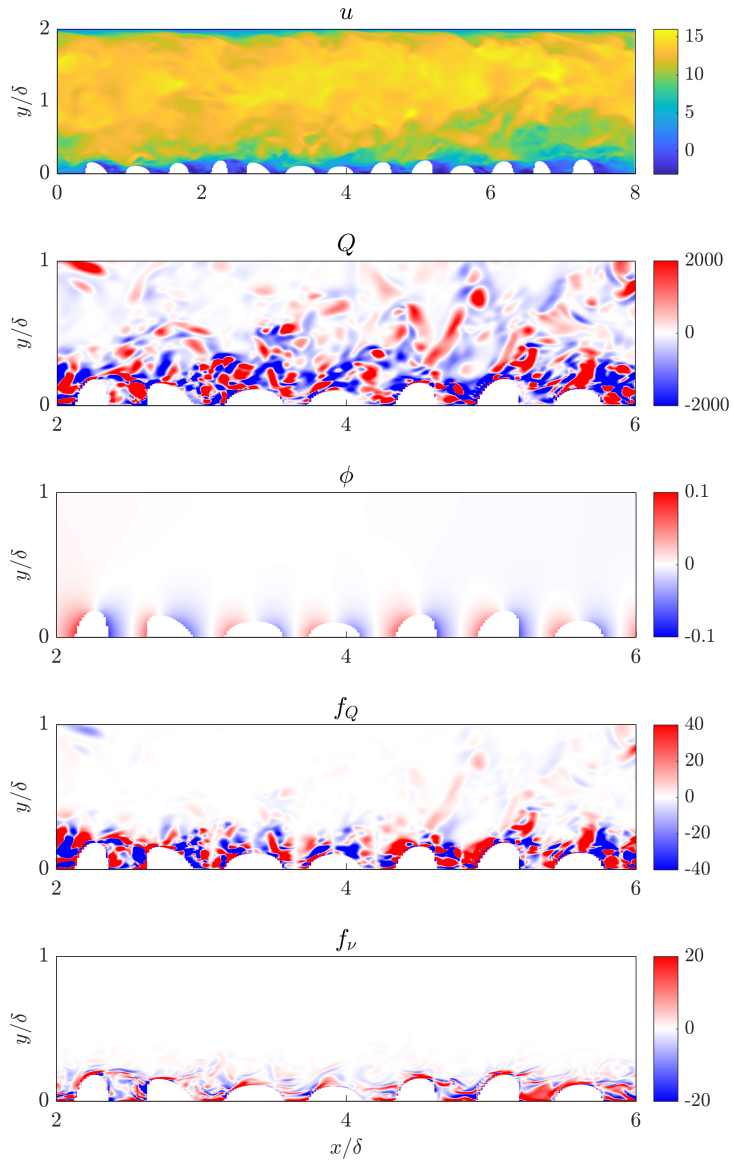


FIG. 9. Contours of instantaneous $u$, $Q$, $\phi$ (constant in time), $f_Q$ and $f_\nu$.

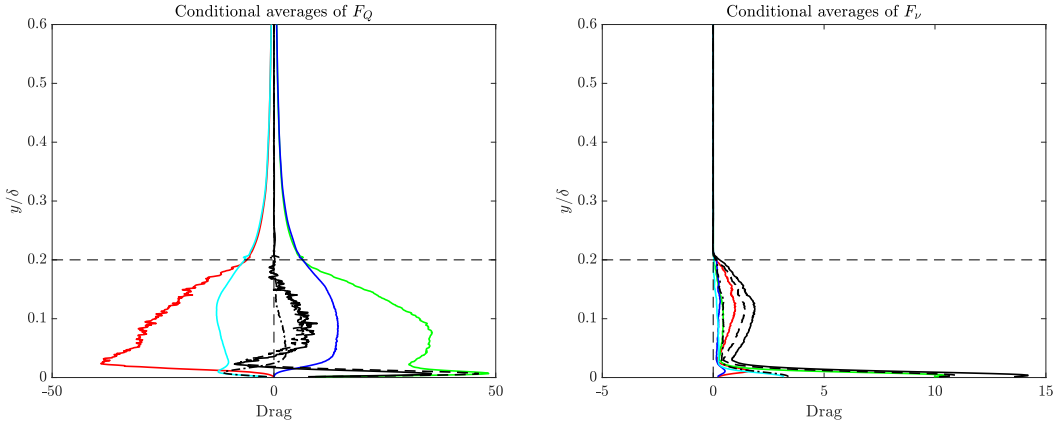


FIG. 10. Weighted conditional averages of $F_Q$ (a) and $F_\nu$ (b) for sand-grain. Legends same as Fig. 5.

## IV. PREDICTION OF EQUIVALENT SANDGRAIN HEIGHT $k_s$ BASED ON $\phi$

It is established that in equilibrium flows with sufficiently high Reynolds numbers for them to be fully rough, the $k_s$ value (representative of the drag-producing capability of a rough surface) depends on the surface geometry only. However, it has been a long-standing challenge to find generally applicable surface parameters and functional forms to describe the dependence of hydrodynamic drag on these parameters. One can describe the roughness function as $\Delta U^+ = \frac{1}{\kappa}\ln(k_s^+) - 3.5$, which characterizes the hydrodynamic drag in fully-rough, fully-developed turbulent channel flows over a rough surface. Equivalently, the roughness length $z_0$ can be determined according to $z_0 = k_s \exp(-8.5\kappa)$ if the equivalent sandgrain roughness is known [10]. However, how these quantities can be related to the actual surface geometry is still an open research topic.

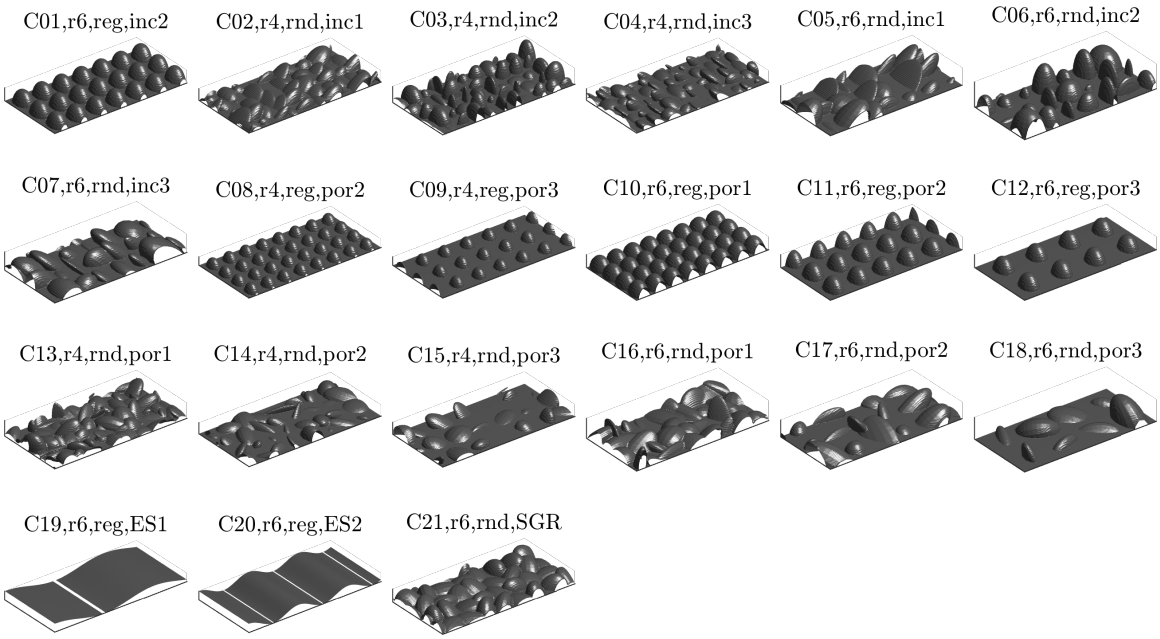


FIG. 11. Roughness database to predict $k_s$, reproduced with permission from [35].

There are extensive studies in the literature that aim to predict $k_s$ based on empirical functions of various roughness geometric parameters that can be defined based on the surface geometry [24, 25, 27]. Recently, Aghaei-Jouybari *et al.* [35] assembled an extensive database (45 surfaces from both new DNSs and existing experiments) to apply Machine Learning techniques such as Deep Neural Networks and Gaussian Process Regression to predict $k_s$ based on a series of surface parameters as inputs. They were able to predict $k_s$ with an average error of less than 10% and a maximum error of less than 30%. The surface characteristics used in prior studies include quantities such as the surface porosity $P_o = \frac{1}{A_t k_c}\int_0^{k_c} A_f dy$ and spanwise effective slope $E_z = \frac{1}{A_t}\int_{x,z}\left|\frac{\partial k}{\partial z}\right| dA$ (see e.g. discussion in [35]). Here we seek to

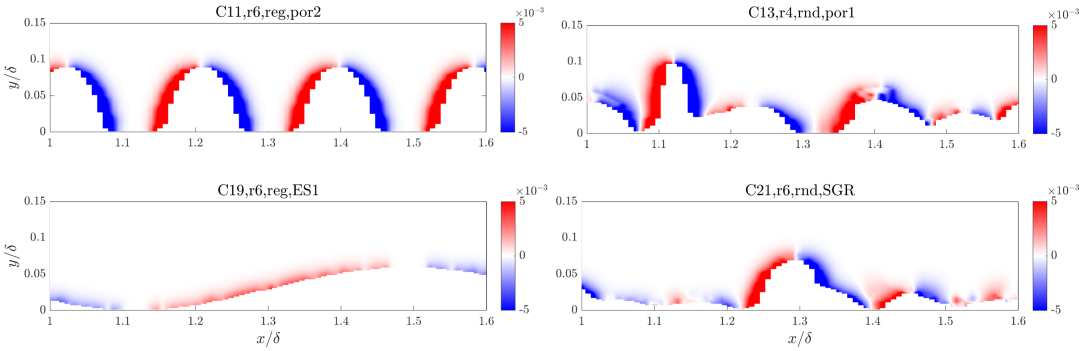


FIG. 12. Calculated $\phi$ field for 4 sample cases from [35]. Only a portion of the domain is shown on a representative $x$-$y$ plane.

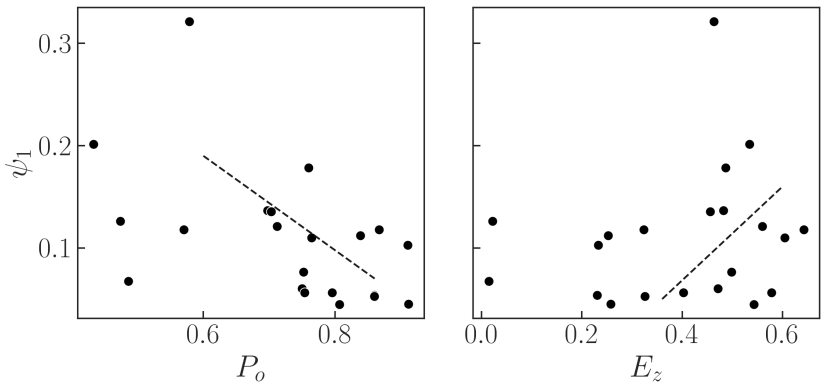


FIG. 13. Scatter plots of the parameter $\psi_1 = \int_0^\infty \langle|\phi|\rangle dy/k_r^2$ against surface geometric parameters: surface porosity $P_o$ (a) and spanwise effective slope $E_z$ (b).

answer the following question: can models for the equivalent sandgrain roughness height be augmented and improved by using characteristics of the $\phi$-field? Recall that the $\phi$-field depends only on the surface geometry and is relatively easy and numerically cheap to compute using any simple Laplace equation solver. As the contours of $\phi$ in Fig. 3 and 9 show, the distribution of $\phi$ appears to contain important additional information about the roughness topography. For instance, depending on how close roughness elements are located from each other, the magnitude of $\phi$ will decrease more or less quickly as one moves away from the surface into the flow domain. Faster decrease can thus be indicative of flow sheltering phenomena behind roughness elements which could thus be associated with reduced average magnitude of $\phi$. In general, $\phi$ contains non-local information about how the surface affects flow in its vicinity. Besides the average magnitude of $\phi$, we will identify two additional quantities that can be defined based on volume integration that provide meaningful additional information that can be used to model $k_s$. By showing that we can establish a correlation between $k_s$ and these three parameters that depend only on $\phi$, we aim to provide empirical evidence that these $\phi$-field properties could be added to traditional parameters (such as surface porosity, effective slope and skewness) for improved modeling of $k_s$.

In order to provide data for our analysis, we use a subset of the DNS database of Aghaei-Jouybari *et al.* [35] in the fully rough regime to explore the prediction of $k_s$ using $\phi$ dependent variables. Twenty one of these surfaces, replotted with permission in Fig. 11, were shown to have $k_s^+ > 70$ (i.e., assumed to be fully rough here) and will be used in the present analysis. Readers are referred to Ref. [35] for in-detail information about the simulations, roughness geometries and calculated $k_s$ values.

We calculated the $\phi$ field for the 21 surfaces. As examples, contour plots of $\phi$ for four samples are shown in Fig. 12. Nominally the $\phi$-field has zero mean when integrating over the flow volume, while the average of its absolute value is non-trivial and may therefore provide useful additional information on which to base models of $k_s$. We first show that while $\phi$ depends solely on the geometry of the surface, it provides information that somewhat differs from traditional geometric parameters even if it displays some correlation with those parameters. For example, consider the $L_1$-norm type dimensionless parameter

$$\psi_1 \equiv \frac{1}{k_r^2}\int_0^\infty \langle|\phi|\rangle dy,$$

where $\langle\cdot\rangle$ represents intrinsic averaging over horizontal planes inside the fluid volume. Note that $\phi$ has unit of length, thus we use the first-order moment of surface height fluctuations $k_r = \frac{1}{A_t}\int_{x,z} |k - k_{avg}| dA$ as characteristic height to normalize all length-scales, similarly done in Ref. [35]. The parameter $\psi_1$ is plotted against the surface porosity $P_o$ and spanwise effective slope $E_z$ in Fig. 13 For moderate and large values of $P_o$ and $E_z$, one notices an overall decreasing trend of $\psi_1$ versus $P_o$ (Fig. 13a) and increasing trend of $\psi_1$ versus $E_z$ (Fig. 13b). Both of these trends are expected: as $P_o$ increases the elements are farther from each other, which leads to a drop of $|\phi|$ in the inter-element regions, and as $E_z$ increases the surface spanwise variation intensifies and results in an increase of $|\phi|$. At low values of $P_o$ (i.e. sparse roughness) and $E_z$ (toward a 2D geometry as $E_z$ approaches zero) the significant scatter seen for $\psi_1$ shows that the $\phi$ field contains additional information regarding the surface not contained simply in the porosity or slope parameters.

The following additional two parameters have shown promising results among a pool of several other candidates

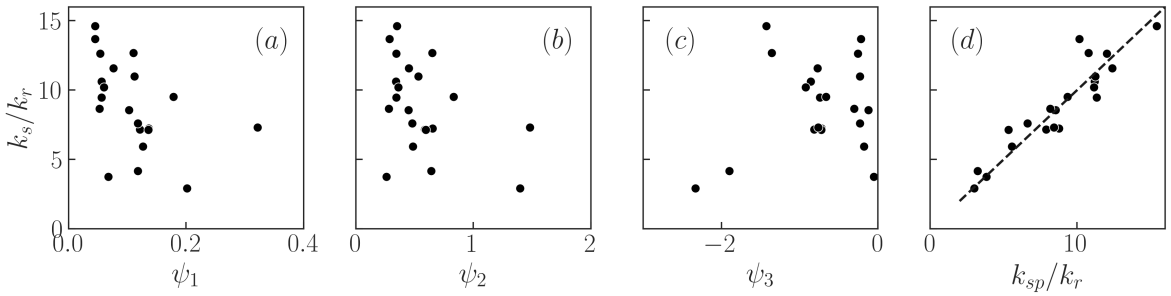


FIG. 14. Normalized sandgrain roughness length as function of the three parameters $\psi_1$ in (a), $\psi_2$ in (b), and $\psi_3$ in (c), and results from three-parameter curve-fitting for which $Err_{avg} = 10.5\%$ and $Err_{max} = 26\%$ in (d).

considered and tested:

$$\psi_2 = \frac{1}{k_r^2}\int_0^\infty \langle |y\boldsymbol{\nabla}\phi| \rangle dy, \tag{4a}$$

$$\psi_3 = k_r \int_0^\infty \langle Q_\phi \rangle \, dy, \tag{4b}$$

where

$$Q_\phi \equiv -\frac{1}{2}\frac{\partial(\partial\phi/\partial x_i)}{\partial x_j}\frac{\partial(\partial\phi/\partial x_j)}{\partial x_i} = -\frac{1}{2}\frac{\partial^2\phi}{\partial x_i\partial x_j}\frac{\partial^2\phi}{\partial x_i\partial x_j} \leq 0.$$

While as described before, $\psi_1$ is the simple normalized average of the absolute value of $\phi$ (using $k_r$ as the normalization length scale) the other two parameters depend upon the spatial gradient of the $\phi$-field. We note that the geometry-dependent vector field $\boldsymbol{u_p} = \boldsymbol{U}_0 - \boldsymbol{\nabla}\phi = \boldsymbol{i} - \boldsymbol{\nabla}\phi$ is the potential flow solution with no-penetration boundary condition for an arbitrary roughness topography (because $\boldsymbol{\nabla}\cdot\boldsymbol{u_p} = 0$, and $\boldsymbol{u_p}\cdot\boldsymbol{n} = 0$ at the solid boundaries, and $\boldsymbol{U}_0 = \boldsymbol{i}$ is the unperturbed velocity of unit magnitude). Thus $|\boldsymbol{\nabla}\phi|$ represents the magnitude of the potential flow velocity deviation from uniform flow caused by the roughness elements. Therefore, the parameter $\psi_2$ is proportional to the average angular momentum flux $y\,U_0\,\boldsymbol{\nabla}\phi$ about the underlying surface at $y = 0$ associated with the potential flow velocity perturbation $\boldsymbol{\nabla}\phi$. For a recent analysis of the importance of angular momentum flux in analysis of skin friction in boundary layers, see Ref. [44] (although there it is the real velocity that is used to define the angular momentum flux which here we cannot use but must use instead potential flow velocity perturbation that can be obtained from the $\phi$-field). Non-dimensionalization with the magnitude of the unperturbed velocity $U_0$ yields the definition as provided in Eq. 4. The parameter $\psi_2$ will be seen, empirically, to correlate well with the drag on the surface.

The third parameter $\psi_3$ is simply the average value of the $Q$ parameter defined based on the potential flow field over the rough surface. It is noted that there is no vortical motion for this potential field, therefore $Q_\phi$ is strictly non-positive and indicative of a pure strain-dominated flow. A number of additional options for $\psi_i$s were considered such as norms based on root-mean-squared of $\phi$, unweighted $|\boldsymbol{\nabla}\phi|$ and others, but they led to less satisfactory results compared to those obtained based on $\psi_1$ to $\psi_3$ above.

Next, a linear and bi-linear relationship is tested, as a simple functional dependence of $k_{sp}$ in terms of the three $\psi_i$ parameters:

$$\frac{k_{sp}}{k_r} = a_1\psi_1 + a_2\psi_2 + a_3\psi_3 + a_4\psi_1\psi_3 + a_5\psi_2\psi_3, \tag{5}$$

where $k_{sp}$ is the model-predicted value of $k_s$ and $a_i$ $(i = 1, \cdots, 5)$ are the empirical coefficients to be obtained via fitting the data. This functional form, comprising 3 linear and 2 bilinear terms, is the simplest polynomial form that yields desirable prediction of $k_s$. The simplicity of this form, with only 5 tuneable coefficients, will prevent the risk of an over-fitted result, however it does not guarantee a positive $k_{sp}$ value in case of extrapolating beyond the training range, in which case a more complex expression must be employed. The empirical coefficients obtained by the curve fitting are $a_1 = -197.0$, $a_2 = 65.85$, $a_3 = -7.358$, $a_4 = 102.0$ and $a_5 = 5.709$.

Figure 14 shows scatter plots of $k_s/k_r$ with respect to $\psi_i$s in subplots (a-c) and also the curve-fitting results in subplot (d). The average and maximum errors of the prediction are 10.5% and 26%, respectively. Here only 5 free variables were used for 21 fully rough surfaces, yet the prediction accuracy is of the same order of the designed DNN

introduced in Ref. [35]. This result strongly suggests that the surface parameters based on $\phi$ are promising to develop drag models for rough surfaces using only geometrical information. The concept of using geometry-dependent fields to help predict $k_s$ could be further generalized. For example, a family of $\phi$ fields could be envisioned, each obtained by using boundary conditions different from those in Eq. (1). These could be chosen to reflect particular properties of the roughness. Also, predictions based on combining the current approach with earlier ones, such as using inputs from the $\phi$ field together with standard statistical features of the roughness geometry (e.g. skewness, slope, porosity, etc..), are interesting and worth examining but are beyond the scope of the present study.

## V. CONCLUDING REMARKS

Identifying sources of the hydrodynamic drag in rough-wall turbulent flows is important for drag prediction, turbulence modeling and control. We employed the force partitioning method to quantify the effect of vortex-dominated ($Q > 0$) and strain-dominated ($Q < 0$) regions on the total drag. The $\phi$ field, which is an important part of the FPM analysis, depends solely on the roughness geometry, and is a signed potential field around roughness elements. A vortex ($Q > 0$) or a strain-dominated region ($Q < 0$) can generate or annihilate the hydrodynamic drag depending on its location in the respective $\phi$ field. As shown in Eq. (3), the pressure drag is decomposed into two terms– $Q$-induced force $F_Q$ and the viscous momentum diffusion induced force $F_\nu$. For a stationary channel flow with cube roughness elements arranged on the bottom wall and smooth top wall at $\mathrm{Re}_\tau = 500$, it was shown that $F_Q$ contributes to the majority of the rough wall drag (52.6%), with other important contributors being $F_\nu$ (22.1%), and the shear forces exerted on both the roughness elements and the smooth portions of the bottom wall (25.3%). The last two factors are expected to contribute less to the total rough wall drag at higher Reynolds numbers. For the same setup but with randomly oriented sand-grain roughness elements, these contributions are 52.7% for $F_Q$, 23.1% for $F_\nu$ and 24.2% for the bottom-wall shear forces, confirming the importance of $Q$-induced motions in rough-wall drag generation for different types of surface topography.

Conditional averages of the $Q$-induced force density, $f_Q = -2\rho Q\phi$, revealed that most of $F_Q$ is generated by the imbalance of strain-dominated regions (contributing to the force) and vortex-dominated regions (opposing the force) upstream of a roughness element, while they cancel each other's effect downstream of a roughness element. Conditional averages of $f_\nu = \mu\nabla^2\boldsymbol{u} \cdot \boldsymbol{\nabla}\phi$ showed a net positive contribution to $F_\nu$ by all events (vortex or strain-dominated) irrespective of their emergence location (upstream or downstream), which was also expected due to irreversible nature of molecular diffusion. We also decomposed $f_{\overline{Q}}$ based on its mean and turbulence components $f_{Q_{uavg}}$ and $f_{Q_{urms}}$ for the cube roughness. The results indicated that for the cube roughness case, about 56% of $F_Q$ originates from the time-mean motions (i.e. contribution from $\overline{Q}_{uavg} = -0.5\overline{u}_{i,j}\overline{u}_{j,i}$). These motions may include head-down $U$-shape structures that occur around $y = 0.5k_c$ and roller structures that occur right on the crest $y = k_c$. The other 44% is due to small-scale turbulent motions i.e. contribution by $f_{Q_{urms}}$ (where $\overline{Q}_{urms} = -0.5\overline{u'_{i,j}u'_{j,i}}$).

Considering that the $\phi$ field depends solely on the roughness geometry and contains also non-local effect caused by the roughness elements on the flow, we explored different parameters associated to the spatial distribution of $\phi$ and attempted to build an empirical correlation to predict the roughness equivalent sandgrain height $k_s$. Our prediction, based on three $\phi$-dependent parameters, offers an accuracy of about 10.5% of the average error and maximum error of 26%. These results were obtained from a database consisting 21 fully rough flows. The model correlation introduced in this study (Eq. 5) employs 5 free parameters (obtained by curve fitting) yet offers an accuracy that is of similar order to that of the deep neural network proposed in [35]. Altogether, this is an indication that information embedded in the $\phi$-field can be used to predict the hydrodynamic drag of rough-wall turbulent flows and can be included in addition to other traditional parameters such as porosity, surface slope and skewness. It must be kept in mind that while such procedures require solution of a Partial Differential Equation (PDE) in the flow volume for each surface, the PDE is a simple Laplace equation, far simpler and inexpensive to solve than performing costly DNS, LES or experimental measurements.

## ACKNOWLEDGEMENTS:

This work is supported by the National Science Foundation (grant CBET-1738918). Computational resources were provided by XSEDE (project TG-ATM130032) and MARCC.



[1] M. R. Raupach and R. H. Shaw, Averaging procedures for flow within vegetation canopies, Bound.-Lay. Meteorol. **22**, 79 (1982)

[2] J. Finnigan, Turbulence in plant canopies, Annu. Rev. Fluid Mech. **32**, 519 (2000)

[3] G. S. Williams and A. Hazen, *Hydraulic tables; the elements of gagings and the friction of water flowing in pipes, aqueducts, sewers, etc. as determined by the Hazen and Williams formula and the flow of water over sharp-edged and irregular weirs, and the quantity discharged, as determined by Bazin's formula and experimental investigations upon large models* (J. Wiley & sons, New York, 1909)

[4] F. Farshad, H. Rieke, and J. Garber, New developments in surface roughness measurements, characterization, and modeling fluid flow in pipe, J. Pet. Sci. Eng. **29**, 139 (2001)

[5] L. Shu, H. Li, Q. Hu, X. Jiang, G. Qiu, G. McClure, and H. Yang, Study of ice accretion feature and power characteristics of wind turbines at natural icing environment, Cold Regions Science and Technology **147**, 45 (2018)

[6] F. Canovaro, E. Paris, and L. Solari, Effects of macro-scale bed roughness geometry on flow resistance, Water Resour. Res. **43** (2007)

[7] S. P. Schneider, Effects of roughness on hypersonic boundary-layer transition, J. Spacecr. Rockets **45**, 193 (2008)

[8] K. S. Cunningham and A. I. Gotlieb, The role of shear stress in the pathogenesis of atherosclerosis, Lab. Investig. **85**, 9 (2005)

[9] M. Schultz and K. Flack, Turbulent boundary layers on a systematically varied rough wall, Phys. Fluids **21**, 015104 (2009)

[10] J. Jiménez, Turbulent flows over rough walls, Annu. Rev. Fluid Mech. **36**, 173 (2004)

[11] A. Busse, M. Thakkar, and N. Sandham, Reynolds-number dependence of the near-wall flow over irregular rough surfaces, Journal of Fluid Mechanics **810**, 196–224 (2017)

[12] Y. Kuwata and R. Nagura, Direct numerical simulation on the effects of surface slope and skewness on rough-wall turbulence, Physics of Fluids **32**, 105113 (2020)

[13] F. Alves-Portela, A. Busse, and N. D. Sandham, Numerical study of fourier-filtered rough surfaces, Phys. Rev. Fluids **6**, 084606 (2021)

[14] J. C. Wu, Theory for aerodynamic force and moment in viscous flows, AIAA Journal **19**, 432 (1981)

[15] L. Quartapelle and M. Napolitano, Force and moment in incompressible flows, AIAA Journal **21**, 911 (1983)

[16] C. Zhang, T. L. Hedrick, and R. Mittal, Centripetal acceleration reaction: An effective and robust mechanism for flapping flight in insects, PLOS ONE **10**, 1 (2015)

[17] K. Menon and R. Mittal, Significance of the strain-dominated region around a vortex on induced aerodynamic loads, Journal of Fluid Mechanics **918**, R3 (2021)

[18] J. Nikuradse, Laws of flow in rough pipes, NACA Technical Memorandum 1292 (1933)

[19] L. Moody, Friction factors for pipe flow, ASME Trans. **66**, 671 (1944)

[20] C. Colebrook, Turbulent flow in pipes, with particular reference to the transition region between the smooth and rough pipe laws, Journal of the Institution of Civil Engineers **11**, 133 (1939)

[21] A. Jain, Accurate explicit equation for friction factor, Journal of the Hydraulics Division **102**, 674 (1976)

[22] D. J. Zigrang and N. D. Sylvester, A Review of Explicit Friction Factor Equations, Journal of Energy Resources Technology **107**, 280 (1985)

[23] L. Kaczmarek, Nonlinear effects of waves and currents on moveable bed roughness and friction , Archives of Hydro-Engineering and Environmental Mechanics **42**, 3 (1995)

[24] J. A. van Rij, B. J. Belnap, and P. M. Ligrani, Analysis and experiments on three-dimensional, irregular surface roughness, J. Fluids Eng. **124**, 671 (2002)

[25] K. A. Flack and M. P. Schultz, Review of hydraulic roughness scales in the fully rough regime, J. Fluids Eng. **132**, 041203 (2010)

[26] J. Yuan and U. Piomelli, Estimation and prediction of the roughness function on realistic surfaces, J. Turbul. **15**, 350 (2014)

[27] P. Forooghi, A. Stroh, F. Magagnato, S. Jakirlic, and B. Frohnapfel, Toward a universal roughness correlation, J. Fluids Eng. **139**, 121201 (2017)

[28] J. W. Deardorff, Three-dimensional numerical study of the height and mean structure of a heated planetary boundary layer, Boundary-Layer Meteorology **7**, 81 (1974)

[29] C. Moeng, A large-eddy-simulation model for the study of planetary boundary-layer turbulence, Journal of Atmospheric Sciences **41**, 2052 (1984)

[30] P. J. Mason, Large-eddy simulation: A critical review of the technique, Quarterly Journal of the Royal Meteorological Society **120**, 1 (1994)

[31] K. A. Flack, Moving beyond Moody, J. Fluid Mech. **842**, 1 (2018)

[32] H. Lettau, Note on aerodynamic roughness-parameter estimation on the basis of roughness-element description, Journal of Applied Meteorology (1962-1982) **8**, 828 (1969)
[33] R. Macdonald, R. Griffiths, and D. Hall, An improved method for the estimation of surface roughness of obstacle arrays, Atmospheric Environment **32**, 1857 (1998)
[34] X. I. A. Yang, J. Sadique, R. Mittal, and C. Meneveau, Exponential roughness layer and analytical model for turbulent boundary layer flow over rectangular-prism roughness elements, Journal of Fluid Mechanics **789**, 127–165 (2016)
[35] M. Aghaei-Jouybari, J. Yuan, G. J. Brereton, and M. S. Murillo, Data-driven prediction of the equivalent sand-grain height in rough-wall turbulent flows, Journal of Fluid Mechanics **912**, A8 (2021)
[36] S. Talapatra and J. Katz, Coherent structures in the inner part of a rough-wall channel flow resolved using holographic piv, J. Fluid Mech. **711**, 161 (2012)
[37] M. Aghaei-Jouybari, G. J. Brereton, and J. Yuan, Turbulence structures over realistic and synthetic wall roughness in open channel flow at $\mathrm{Re}_\tau = 1000$, J. Turbul. **20**, 723 (2019)
[38] R. J. Volino, M. P. Schultz, and K. A. Flack, Turbulence structure in a boundary layer with two-dimensional roughness, J. Fluid Mech. **635**, 75 (2009)
[39] A. A. Townsend, *The structure of turbulent shear flow* (Cambridge University Press, 1976)
[40] R. Mittal, H. Dong, M. Bozkurttas, F. Najjar, A. Vargas, and A. Von Loebbecke, A versatile sharp interface immersed boundary method for incompressible flows with complex boundaries, Journal of computational physics **227**, 4825 (2008)
[41] J. H. Seo and R. Mittal, A sharp-interface immersed boundary method with improved mass conservation and reduced spurious pressure oscillations, Journal of computational physics **230**, 7347 (2011)
[42] X. I. Yang and R. Mittal, Acceleration of the jacobi iterative method by factors exceeding 100 using scheduled relaxation, Journal of Computational Physics **274**, 695 (2014)
[43] P. R. Bandyopadhyay, Rough-wall turbulent boundary layers in the transition regime, J. Fluid Mech. **180**, 231 (1987)
[44] A. Elnahhas and P. L. Johnson, On the enhancement of boundary layer skin friction by turbulence: an angular momentum approach, Journal of Fluid Mechanics **940**, A36 (2022)